Observation of an exotic lattice structure in the transparent $KTa_{1-x}Nb_xO_3$ perovskite supercrystal

Leonardo Lo Presti,[1] Jacopo Parravicini [ORCID],[2,*] Raffaella Soave,[3] Gianbattista Parravicini,[4] Michele Mauri,[2] Laura Loconte [ORCID],[1] Fabrizio Di Mei [ORCID],[5] Ludovica Falsi,[5,6] Luca Tartara,[7] Simona Binetti,[2] Aharon J. Agranat,[8] and Eugenio DelRe[5,9]

[1]*Dipartimento di Chimica, Università degli Studi di Milano, I-20133 Milano, Italy*
[2]*Dipartimento di Scienza dei Materiali, Università di Milano-Bicocca, I-20125 Milano, Italy*
[3]*Istituto di Scienze e Tecnologie Chimiche "Giulio Natta" (SCITEC), Italian CNR, I-20133 Milano, Italy*
[4]*Dipartimento di Fisica, Università di Pavia, I-27100 Pavia, Italy*
[5]*Dipartimento di Fisica, "Sapienza" Università di Roma, I-00185 Roma, Italy*
[6]*Dipartimento S.B.A.I., Sezione di Fisica, "Sapienza" Università di Roma, I-00161 Roma, Italy*
[7]*Dipartimento di Ingegneria Industriale e dell'Informazione, Università di Pavia, I-27100 Pavia, Italy*
[8]*Applied Physics Department, Hebrew University of Jerusalem, IL-91904 Jerusalem, Israel*
[9]*ISC-CNR, "Sapienza" Università di Roma, I-00185 Roma, Italy*

We perform redundant x-ray diffraction versus temperature experiments in bulk transparent KTN. We find a violation of the standard perovskite cubic-to-tetragonal symmetry breaking at the Curie point in the form of an orthorhombic cell distortion. The lattice distortion spans coherently macroscopic volumes of the sample and is characterized by a negative-to-zero thermal volume expansion. Dielectric measurements and calorimetry indicate that the anomalous behavior is not associated to a distinct thermodynamic phase. The comparison of linear and nonlinear optical scattering experiments with structural data suggests that the lattice distortion is a consequence of strain relaxation to a 3D superlattice of polarization vortices.

Introduction. A wide variety of innovative materials for a range of applications have a perovskite atomic structure. Examples are high-temperature and anomalous superconductors, photovoltaics, and a host of solids with unconventional and giant electromechanical, capacitive, piezoelectric, magnetoresistive, thermal, and optical response [1–11]. While new functional materials with a perovskite structure are still being discovered and engineered, many useful effects still have no general explanatory picture, making the whole subject matter an attractive riddle-ridden arena for condensed matter physics [12–14].

An interesting effect is observed in transparent solid-solution KTN perovskites cooled below their room-temperature Curie point. Specifically, illuminating the sample with plane-wave laser beams leads to far-field diffraction patterns typical of three-dimensional photonic crystals with a micrometric lattice constant [15–17]. Remarkably, focusing light into a single lattice site causes it to refract and diffract as if it had a broadband giant index of refraction (GR) [8,11]. The effect is thought to be connected with the formation of a ferroelectric supercrystal (SC), a 3D periodic domain mosaic of interwoven polarization vortices, each lattice site being the crossing of six polarization vortex cores (a hypervortex). While numerous results are being found associated to the macroscopic optical, dielectric, and piezoelectric response, little is as yet known of the effect the

coherent micrometer-scale domain mosaic has on the average atomic structure.

We performed an in-depth 3D structural investigation of bulk KTN cooled below its Curie point using x-ray diffraction data. To correlate average atomic structure data to macroscopic (micrometer and above) SC patterns, we also performed optical diffraction, optical second-harmonic generation, dielectric measurements, and calorimetry measurements. Results indicate that the emergence of the ordered 3D ferroelectric cluster patterns is accompanied by a previously unreported large scale and coherent lattice deformation. The signature is that the standard perovskite sequence of lattice symmetries on cooling, i.e., cubic-to-tetragonal, tetragonal-to-orthorhombic, orthorhombic-to-rhombohedral [18], is transformed to cubic-to-orthorhombic, orthorhombic-to-tetragonal, and tetragonal-to-rhombohedral. In our modeling, we describe how this unconventional deformation in the average atomic structure is compatible with the strain field caused by the vortex polar domain distribution typical of a SC.

Materials. A single-crystal solid-solution KTN ($KTa_{1-x}Nb_xO_3$, $x = 0.36$) compound was grown through the top-seeded solution method. The concentration of potassium, tantalum, and niobium in the crystal was determined by electron microprobe analysis. Two *c*-direction-pulled zero-cut samples are extracted from the original rod, a $1.8 \times 1.8 \times 2.3$ mm specimen to perform dielectric spectroscopy measurements, and a $0.5 \times 0.5 \times 1.6$ mm specimen that formed the starting batch material for x-ray
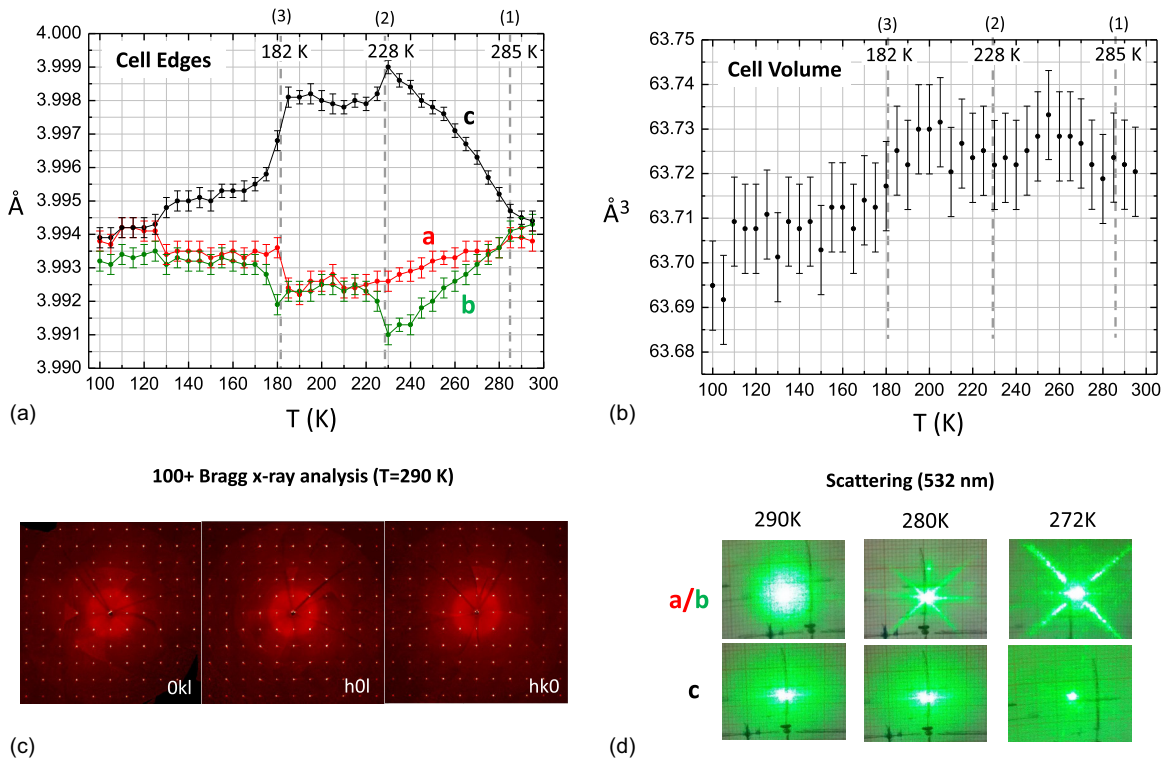
*jacopo.parravicini@unimib.it

FIG. 1. Coherent lattice distortion in ferroelectric KTN. (a) Cell edge lengths (Å), *a* (red dots), *b* (green rhombi), and *c* (blue triangles) of KTN as a function of *T*. Each point was estimated by single-crystal x-ray diffraction from a least-squares fitting against ∼110 reflections within $2\theta \simeq 34°$. Error bars correspond to one estimated standard deviation (e.s.d.). Vertical dashed lines mark the first-order phase transitions that were detected by differential scanning calorimetry (DSC) and dielectric spectroscopy (see Fig. 3). (b) Volume (Å³) of the crystallographic unit cell of KTN as a function of *T*. Due to the anisotropic response of the cell axes, the overall thermal expansion is zero down to the low-*T* transition at 182 K. (c) Reconstructed precession images of three equatorial sections of the KTN reciprocal lattice at room temperature, as viewed down the a^*, b^*, and c^* reciprocal cell edges. Changes in the positions of the peaks as the sample is cooled down are not appreciable by the naked eye. (d) Output of light scattering experiments close to the Curie point.

diffraction (XRD) and calorimetry (DSC) measurements. Second-harmonic-generation (SHG) experiments are performed in a $7.0 \times 3.9 \times 1.6$ mm sample designed to have a higher T_C ($T_C = 333$ K) adding a small concentration (<0.01) of Li to the melt (KTN:Li). As for many composite nonstoichiometric samples, the deposition process introduces slight oscillations in the composition that lead to so-called striations. The micrometric scale of these striations is thought to form the precursor of ferroelectric supercrystals [8,15].

X-ray diffraction. A 100+ Bragg-peak x-ray 3D structural investigation of a single-crystal KTN is reported in Figs. 1(a)–1(c). The starting batch consisted of a transparent, hard, and brittle mm-long rod of the freshly synthesized KTN material. The opposite extremities were cut with a stainless steel microblade. Irregular crystals of micrometer dimensions were obtained. Twelve of them were discarded after preliminary checks due to heavy twinning. Eventually, one high-quality nonpleochroic specimen was selected for the data collection. The linear size does not exceed 100 μm to alleviate the very high absorption of KTN ($\mu \simeq 29$ mm^{-1}) at the x-ray wavelength here employed ($\lambda = 0.71073$ Å). Each crystal was mounted on the top of a glass capillary fiber with bi-component epoxy glue and placed in very close proximity of the cold nitrogen nozzle. A three-circle Bruker AXS Smart diffractometer equipped with an APEX II CCD detector and

an Oxford Cryosystem N_2 gas blower was used throughout. Graphite-monochromated Mo K$_\alpha$ radiation ($\lambda = 0.71073$ Å) at a nominal power of the generator of 50 kV × 30 mA was employed. Diffraction amplitudes were collected in the ω-scan mode from the hemisphere up to a maximum Bragg angle of $\simeq 37°$ (area detector fixed at $2\theta = 0°$, sample rotating around the goniometer *z* axis by varying ω) and the temperature was changed stepwise from 295 K to 100 K, with $\Delta T = 5$ K; before starting any data acquisition, the sample was equilibrated in the cold N_2 stream for $\simeq 10'$. Possible hysteresis phenomena were excluded by repeating data collections at specific temperatures after having warmed back the specimen at room temperature [19–23]. Data integration and reduction were carried out by the SAINT+ suite of programs [24]. The detector is positioned 50 mm from the sample: illuminating the whole sample gives an average lattice analysis on the entire sample. The diffraction data were uniformly distributed in the reciprocal lattice up to max[sin(θ)/λ] = 0.45 Å^{-1} (see below), and each of them represents the scattering output from the entire volume of the bulk material. We were thus able to measure very precisely the cell edge length down to 100 K, obtaining for the first time reliable estimates of the *T*-driven lattice distortions in KTN. Eventually, we collected a total of 100+ x-ray Bragg peaks at each temperature. The lattice constants were computed by minimizing the average
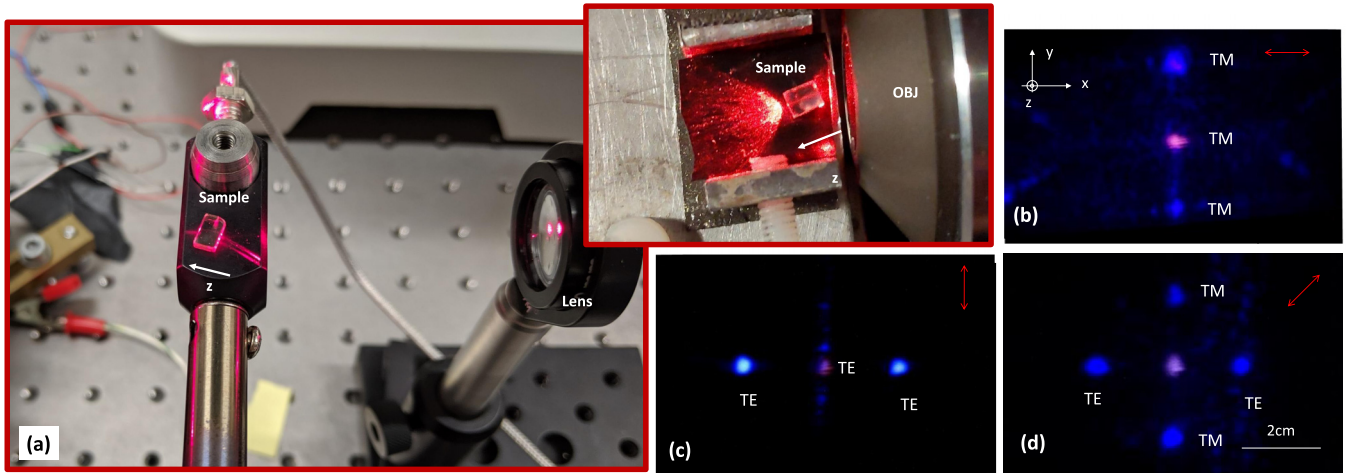
FIG. 2. GR and SHG Experiments. (a) Light is focused onto the input facet into a polarization vortex core, identified using giant refraction (inset). SHG for (b) TM, (c) TE, and (d) a superposition of TM and TE modes maps the signature spatial and polarization structure of the vortex [11].

square deviations between the measured reflection centroids and those predicted on the basis of the lattice model. In the standard least-squares procedure, lattice constants are varied together with instrumental parameters, which include possible detector misplacements and centering errors of the crystal. In KTN, T-driven distortions of cell edge lengths are very small ($\leqslant 0.1\%$) and of the same order of magnitude as the least-squares estimated adjustments affecting the instrumental parameters. This results in high correlations, which imply an odd dependence of the instrumental parameters on the cell edges and vice versa, as well as very high estimated standard deviations of the final least-squares variables. To limit these problems, we measured the positions of the Bragg peaks in the reciprocal reference frame using a very small scan width in ω ($\Delta\omega = 0.15°$). Possible systematic errors in the position of the instrumental zero were minimized by collecting reflections at both positive and negative 2θ. Fast exposure times (3 s/frame) were used to ensure that counting statistics always remain in the linearity region of the CCD detector device. Finally, instrumental parameters were optimized at RT and then kept fixed in least-squares refinements at lower T (more details in the Supplemental Material). This way, the diffraction maxima can be accurately located, even for the most intense reflections. The very low (<0.001) cell microstrain [Figs. 1(a)–1(c)] implies that transition-induced crystal twinning, if any, is not detectable. This is because the associated reciprocal space splitting of the Bragg peaks would be lower than 0.002 rad, corresponding to a deviation comparable with the detector pixel size (0.12 mm). Cell volume across the entire range of inspected temperatures is reported in Fig. 1(b) [19,25–32].

Optical diffraction. The macroscopic formation of extended 3D ferroelectric cluster patterns below T_C in the KTN sample are observed using visible light propagation, as reported in Fig. 1(d) [15]. While domains in KTN can be directly observed using transmission polarization microscopy in thin plates [33], periodic domain patterns in the volume can be optically detected using coherent scattering, as originally demonstrated in KTN by Bouziane *et al.* [34]. We note that the patterns occur spontaneously, i.e., without fabrication or

post-processing protocols (such as laser-induced domain pattern orientation), on cooling through T_C. Light transmission is analyzed illuminating the sample with a polarized plane wave from a frequency-doubled Nd-YAG laser ($\lambda = 532$ nm). Transmitted light parallel to a specific crystal axis is collimated and imaged onto millimeter paper placed after the sample. Different directions are inspected rotating the sample. Crystal temperature in the range 265–300 K is fixed through a water-cooled current-driven Peltier junction placed below the sample holder. Temperatures are measured relative to T_C that is evaluated optically through cross-polarizer transmission microscopy. To avoid strong water condensation, optical diffraction is investigated for temperatures down to 270 K. Optical diffraction patterns are evident for two directions, while the diffraction peaks are accompanied by background scattering. Far-field images provide the angular scale of the Bragg diffraction. The angular peak-to-peak distance identifies a spatial scale $\Lambda \simeq 5.2 \, \mu$m, which is in agreement with the scale of the growth striations associated to the standard bulk sample pulling process [15]. Results are incompatible with propagation through a disordered mosaic of ferroelectric clusters and in agreement with the slow metastable relaxation into the fully ordered 3D SC cluster mosaic previously observed in other samples in the proximity of the Curie point [15].

Second-harmonic generation. The details of the local polar domain structure of the SC are analyzed using SHG experiments in a KTN:Li sample, as reported in Fig. 2 [11]. At room temperature the sample is in its nominal tetragonal phase ($T = T_C - 35$ K) and manifests a 3D SC. The sample gives rise to giant refraction as shown in the inset of Fig. 2(a), where laser light from a supercontinuum source is launched at $\lambda = 650$ nm from a large-aperture objective. SHG experiments are carried out using a Tsunami Spectra Physics Ti:Sa CW mode-locked laser at $\lambda = 810 \pm 7$ nm, operating at 0.6 W, with a repetition rate of 80 MHz and a pulsewidth of 190 fs. Laser beam linear polarization, transverse magnetic (TM), or transverse electric (TE), or a superposition of the two, is set rotating a $\lambda/2$ waveplate. The beam is then
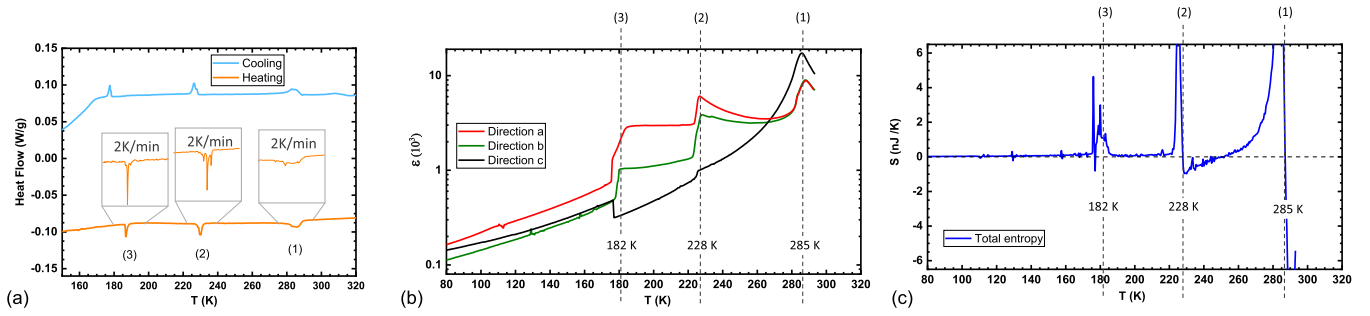
FIG. 3. Macroscopic response. (a) DSC thermogram of KTN in the 143 K-RT range of T; (1), (2), and (3) indicate endothermic first-order phenomena at 285, 228, and 182 K. Insets represent a closeup of the transitions when studied at 2 K/min. (b) Dielectric response as a function of T along three orthogonal main crystalline axes at the sample frequency of 10 kHz. (c) Total entropy calculated through the sum of the induced Fröhlich entropy $S_E = S_E(T)$ along the three crystalline axes [74–76] as a function of T [19].

focused onto the input facet of the sample using a 50-mm-focal-length lens [Fig. 2(a)]. The pump beam is focused to a FWHM $\simeq$15 μm and is launched inside a SC lattice site appropriately positioned and rotating the sample. The SHG pattern is detected on a white screen placed at $d = 7.0$ cm from the output facet of the sample using a Canon EOS 50d. A polarized SHG signal peaked at $\lambda = 405$ nm is detected both for transverse magnetic (TM) [Fig. 2(b)] and transverse electric (TE) [Fig. 2(c)] pump modes. For the TM polarized pump, two SH beams emerge in the x-y plane at an angle $\theta_C = \arccos{(2k_1/k_2)} \simeq 0.28$ rad with respect to the pump, where k_1 and k_2 are, respectively, the wave vectors of the fundamental and the SH beams. The SHG output intensity distribution is reported in Fig. 2(b), where both Cerenkov beams are TM. For a TE pump, two TE SHG beams emerge in the x-z plane [Fig. 2(c)]. A pump linearly polarized at 45 degrees (i.e., $(|TM\rangle + |TE\rangle)/\sqrt{2}$), leads to the diamondlike SHG pattern in Fig. 2(d). Cerenkov SHG forms four polarized beams, where the beams along the y direction are TM, and those in the x direction are TE.

Calorimetry. Calorimetric measurements of the KTN sample are reported in Fig. 3(a). Differential scanning calorimetric (DSC) measurements were carried out in the 143 K-room-temperature (RT) range using a Mettler Toledo DSC1 apparatus with Star^e software (version 11.0). The entire crystal was placed into a 40 μl aluminum pan, carefully positioned flat on the bottom in order to maximize heat transfer with the instrument. The sample is thermalized 5 minutes at 143 K, heated to 323 K, and finally cooled back to 143 K at 2, 5, 10, and 15 K/min rate. Sharp transitions were located by averaging the onset temperature measured during heating and cooling ramps at various rates [35–37].

Dielectric measurements. Dielectric response for the KTN sample in the 80–295 K range is reported in Fig. 3(b). The real part of the permittivity versus temperature T is measured by a precision LCR meter (Agilent-4284A) applying a probing electric field of 1 V/cm between plane parallel electrodes deposited on the sample facets. Temperature variation in the 75–320 K range is obtained employing a closed two-stage helium cryostat. The thermal variation rate is 1 K/min and monitored through a calibrated silicon diode sensor (0.01 K in precision). The dielectric response is measured along the three crystalline main directions a, b, c, in three different consecutive scan stages, keeping all experimental parameters constant,

especially the thermal variation rate and the strength of the probing field. Each set of measurements is carried out for the frequencies 1, 10, 100, and 1000 kHz and the acquisition rate is two measurement points for 1 K [19,38,39].

Discussion. Cell-size analysis for the KTN sample reported in Fig. 1(a) indicates that while the standard cubic to tetragonal transition is observed in cooling the sample below $T_C = 285$ K, this symmetry is superseded at 270 K by a stable orthorhombic distortion that persists to lower temperatures, down to $\simeq$230 K. Here, cooling below $T = 228$ K, symmetry is found to increase as a low-T tetragonal phase emerges from the high-T orthorhombic one. Since the statistical significance of the observed distortion of the unit cell refers to a redundant analysis of Bragg peaks, each collecting the scattering contribution from the whole sample, this implies that the lattice distortion, which includes the anomalous increase in symmetry on cooling, coherently pervades the entire bulk material.

An increase in symmetry on cooling is not forbidden on absolute grounds. In fact, according to group theory, it is only required that low-symmetry phases lie both in a symmetry subgroup of the high-T prototype one [40]. Even so, while short-range distortions are known to locally lower the symmetry, it is unusual to observe an increase in long-range symmetry upon cooling in the context of perovskite research. In detail, mainstream theories, including the Landau theory, describe nonreconstructive structural phase transitions in homogeneous systems identifying an order parameter. Experimentally, such transitions imply the occurrence of a symmetry relationship relating the involved phases. In ferroic transformations, like in ferroelectrics, this relationship is strictly a point group-subgroup one. According to Aizu [41] (and references therein), the crystal structures of transition-related phases must all be described by slight distortions of a prototype reference structure, necessarily the most symmetric one. A distortion here means that the ferroelectric phase (the low-T one, i.e., that existing below the Curie temperature) is expected to bear a lower symmetry, i.e., to belong to a point group of lower order. Mixed perovskites, in turn, such as the Mg/Pb niobates that have attracted continued attention in recent years, are known to be chemically and structurally heterogeneous on different length scales at the same time [31]. This leads to an anomalous physical response, over a broad range of temperatures, that cannot be fully described by a Landau-like approach. For one,

no obvious order parameter can be identified. As regards specifically to our results in KTN, the phase sequence from RT to 100 K [Fig. 1(a)] is cubic-orthorhombic-tetragonal-tetragonal-rhombohedral, which corresponds to an alleged sequence of point groups $m3m \supset [mm2 \subset (4mm = 4mm \supset 3m)]$. All the low-$T$ phases thus belong to a subgroup of the prototype $m3m$ one, a circumstance that apparently agrees with the Aizu paradigm. In fact, two fundamental differences emerge: First, a nonferroic transition occurs at low T, which relates two different tetragonal ferroelectric phases; second, all the phases below ~230 K are supergroups of $mm2$, the one appearing just below the Curie point. To the best of our knowledge, this phenomenon has never been reported for $BaTiO_3$ and $BaTiO_3$-type single-crystal ferroelectric materials, which rather follow the expected sequence $m3m \supset [4mm \supset (mm2 \subset 3m)]$. That is, in ordinary perovskite ferroelectrics the low T $mm2$ and $3m$ phases can also be rationalized as small distortions of a prototype ferroelectric phase (4mm). Rather, in KTN, the only meaningful prototype is the paraelectric cubic one ($m3m$), implying that, below the Curie point, a very strong and unexpected cubic to orthorhombic symmetry breaking occurs.

Unexpected XRD findings can arise as artifacts of apparent pseudosymmetries generated by a crystallographic multidomain structure. To exclude this and ensure that we were observing an actual spontaneous symmetry breaking at the atomic scale (followed by the significant symmetry gain on cooling), we took great care in selecting true single crystals, that is, crystallographically homogeneous (single-lattice) specimens. For sure, grain boundaries and extended defects exist in our specimens, but in a much lower concentration than in a multidomain system (twinned, powdered). Moreover, x-ray diffraction outcomes (Fig. 1(c) and Ref. [19]) confirm that lattice parameters have the same orientation throughout the whole bulk sample, that is, defect-bounded crystallites are all iso-oriented.

Anomalous symmetrization could be associated to a so-called reentrant transition, a thermodynamic characterization that is, in our case, not applicable. First, it is not obvious what order parameter should be defined in the allegedly "ordered" orthorhombic phase, as KTN is an intrinsically disordered solid solution already at high T. The disorder in KTN is occupational and temperature invariant. Moreover, the very small distortions of the cell parameters (Fig. 1 and Ref. [19]) ensure that atomic displacement is too small to produce a significant entropic drive for the transition. Finally, DSC results (3) point out that the first-order transitions we detect upon cooling are all endothermic ($\Delta H > 0$). Accordingly, this implies that some "hidden mechanism" should exist to allow for the spontaneity of the process ($\Delta G < 0$) [42].

Supercrystal model. While theoretically possible, the switching of orthorhombic and tetragonal phases upon cooling is anomalous and bears deep physical and chemical significance. In what follows we discuss how the 3D SC model is able to provide an interpretative picture of XRD data corroborated by the optical diffraction, dielectric spectroscopy, and calorimetry measurements. Ferroelectric perovskites suffer a spontaneous symmetry breaking from the cubic phase to the polar tetragonal phase at T_C. Here a strong spontaneous polarization emerges along one of the six principal crystal

axes [18,43,44]. As a textbook example of a solid-solid phase transition, the passage from the nonpolar or paraelectric phase to the polar or ferroelectric phase has always been thought to spontaneously give rise to a disordered distribution of polar domains in which free energy is minimized taking into account both defects, inhomogeneities, and the actual finite size and shape of the sample [31,45]. Optical scattering experiments in bulk KTN:Li samples suggest an entirely different picture [15,16]. To explain what can best be described as the optical equivalent of x-ray diffraction from a crystal lattice, polar clusters appear to spontaneously organize into a macroscopic coherent 3D mosaic with a micrometric periodicity, the ferroelectric SC. A model for the phenomenon is based on the formation of a superlattice of polarization vortices. A polarization vortex is a topological defect that emerges in reaching a state of equilibrium from the nonpolar to the polar phase [see illustration in Fig. 4(a)]. In detail, the reduction of volume/surface charge and strain leads to two basic polarization domain patterns, the 180° alternate domain sequence with a domain wall parallel to the crystal axes, and the 90° pattern, in which the wall is at 45° to the crystal axes. These two types of patterns will in general combine into complex patterns with a rich and varied phenomenology [45,46]. The vortex is now a combination of four separate domains with a spontaneous polarization that wraps around a localized singularity where the four 45°-oriented domain walls meet. Even though strain compatibility reduces stress at each domain wall [47], the vortex structure can cause a rotational stress associated to a finite toroidal moment that can dominate response close to the Curie point [48].

Polarization vortices in the bulk, in thin and layered geometries, are known to remain stable even below the Curie point, both as single isolated defects and in large arrays of stacked two-dimensional superlattices [8,15,49,50]. In these, they appear as reconfigurable localized domain structures for electrically controllable energy and information storage and processing [see illustration of the 2D SC in Fig. 4(b)]. As a result of a combination of tetragonal units, each vortex has an equally elaborate associated strain configuration that also depends on its surroundings, a phenomenon typically used to encode ferroelectric memory devices [51].

Numerical studies of perovskites in the tetragonal phase indicate that vortex structures are stable also in volume systems with no dominant external stimuli [52]. The formation of the 3D SC is then modeled as the 3D generalization of the 2D SC to 3D, as illustrated in Fig. 4(c). The screening of volume and surface charge causes the tetragonal domains to combine into a cubelike structure formed by six independent vortices. In these terms, each unit cell of the 3D SC has an associated stress field caused by the specific combination of the single component vorticities. Combining different types of unit cells, it is possible to design cubic, polar, and even orthorhombic strain fields from a single tetragonal building block [see Fig. 4(d)]. Hence, the exotic lattice structure can arise as a result of the anisotropic 3D stress field that accompanies the specific 3D polar cluster configuration. The effect also dominates the cell structure below the second phase transition, at 228 K, where the perovskite passes from an orthorhombic to a tetragonal phase. Here the natural orthorhombic phase [18,32] is superseded by an anomalous tetragonal phase below
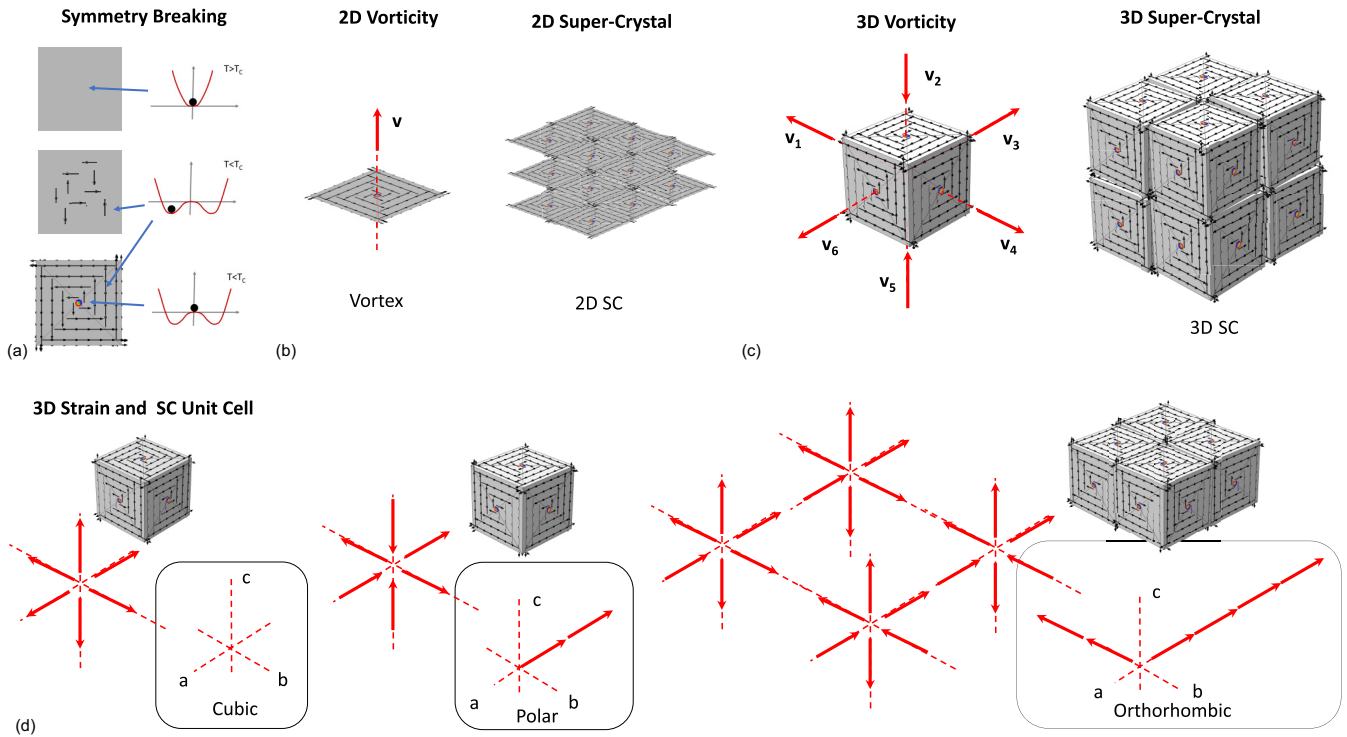
FIG. 4. The 3D SC model and a possible origin of the anisotropic strain field. (a) Spontaneous polarization (black arrows) is formed as the Gibbs potential G vs P (dark red curve) passes from having a single minimum (top row) to having a characteristic double minimum below the Curie point at $T = T_C$ (center). The resulting multidomain structure expands and preserves an unpolarized state in the form of a topological defect vortex (bottom). Since spontaneous polarization can only form along the crystal principal axes, the physics resembles that of Heisenberg magnets. (b) In 2D, topological defects inherit a higher-dimensional 3D vortex structure (left) that can then form a 2D SC (right). The red vector **v** represents the local vorticity of the polarization field [19]. (c) In the volume, defects inherit a 4D structure, forming a 3D hypervortex (left), that can then form 3D SCs (right). D) Each unit hypervortex (left) is formed by six independent vortices that wrap around the central point. These can combine to form SC unit cells with a resulting strain field (boxed panels) that can be both cubic (left, zero strain along a, b, c), polar (center, $+2$ strain along a, zero strain along b, c), and orthorhombic (right, $+4$ along a, $+2$ along b, zero along c). Since each component vortex has an associated strain principally in the plane orthogonal to its vorticity vector, in the orthorhombic case we expect a larger lattice distortion along one specific axis (i.e., the c direction).

210 K. This anomaly, that persists down to the third phase-transition temperature at 182 K, would then be the result of the stress field associated to having the single constituent parts of the SC pass from the tetragonal to the orthorhombic phase. In other words, the SC leads to an orthorhombic strain field when it is made of tetragonal units, while it leads to a tetragonal strain field when it is made of orthorhombic unit solids. The model is discussed in Ref. [19].

The average distortions we report are smaller than the uncertainty of previous studies [32,53,54]. These have, congruently, failed to identify the structural anomaly reported in Fig. 1(a). While this may reflect a strain-stress mechanism specific to the family of KTN samples inspected, or even the specific composition of our samples, it could equally represent a general trait common to other perovskites. This is because previous studies performed XRD monitoring a limited number of reflections, and if single-crystal x-ray and neutron detection is limited to the monitoring of a small number of reflections, no significant evidence of a shift from the basic high-temperature cubic lattice can be observed [19,54–56]. In other words, the lattice distortions reported in Figs. 1(a) and 1(b) are detected only when the number of accurately measured Bragg peaks is radically increased. In any case,

the distortions here discussed are also composition dependent to some extent, as the phase sequence in perovskite solid solutions often changes with composition. The present results should thus encourage us to perform accurate single crystal x-ray diffraction experiments to check whether and to what extent these structural transitions are common in the KTN class of materials.

As reported in Fig. 1(b), the exotic orthorhombic phase from 270 K to 228 K and the exotic tetragonal phase from 210 K to 182 K are accompanied by an anomalous compressibility. The macroscopic thermal response is strongly anisotropic, as one unit cell vector undergoes a large negative thermal expansion [$\alpha_p(c) = -1.95(1) \times 10^{-5}$ K^{-1}]. The result is a material with an overall negligible thermal expansion [$\alpha_p(V) = +1.78(1) \times 10^{-8}$ K^{-1}] over the whole 100 K range and a zero thermal expansion in the 182–285 K region. In terms of the 3D SC strain-stress field, this may be a manifestation in 3D of the negative linear response observed in layered 2D systems where the inverted potential at the vortex core [see Fig. 4(a), bottom] leads to negative capacitance [57,58].

The physical picture is corroborated by the optical diffraction experiments reported in Fig. 1(d) and the SHG experiments in Fig. 2. In fact, for temperatures slightly above

and below the point at which the lattice anomaly occurs, the characteristic optical Bragg diffraction that accompanies the emergent SC is found. In turn, the SHG emerges as highly structured and polarization-dependent Cerenkov radiation [59,60], a direct signature of an underlying organized polar cluster structure specific to the 3D SC [19].

The picture is further supported repeating the XRD analysis for different portions of the original bulk crystal. Cell edge vs T anomalies are found to have different onset temperatures [19,61–64], indicating that the effect is driven by defects and inhomogeneities specific to the sample, as expected to occur in the formation of the 3D SC [15].

On a macroscopic scale, the idea that a strain field associated to the 3D SC drives the anomalous cell behavior implies that the underlying perovskite suffers a standard sequence of phase transitions at the three critical temperature T_1, T_2, T_3. This is confirmed through calorimetric measurements of the material reported in Fig. 3(a) that show a standard sequence of three solid-solid transitions typical of perovskites. Specifically, no latent heat is found in the regions between 285 and 228 K and 210 and 185 K, where the anomalous lattice structure emerges (see Fig. 1), this excluding a first-order phase transition. The absence of a temperature resonance in the dielectric response in the 285–228 K range reported Fig. 3(b) also excludes a second-order type transition [65]. In other words, the passage below 285 K from the tetragonal to the orthorhombic structure does not occur through a transition but through an ordering of tetragonal clusters into the model 3D SC (and equally for the second orthorhombic to tetragonal anomaly below 210 K) [66]. Dielectric measurements further reveal strong differences along the three principal perovskite axes a, b, and c in the relative real permittivity $\epsilon = \epsilon(T)$ [Fig. 3(b)]. Since permittivity for polydomains samples is strongly affected by domains size, orientations, by domain walls, and even domain wall motion [53], this macroscopic anisotropy corroborates the idea of an anisotropic ferroelectric domain distribution typical of the 3D SC. The response analyzed in terms of dielectric or Fröhlich entropy (see Fig. 3(c) and Refs. [19,67–73]) indicates a temperature interval that overlaps with the 3D SC hypothesis (230–250 K) in which the reorientational entropy changes sign far from the critical points T_1 and T_2 [74–76]. This agrees with the scenario described in Fig. 4(e) (right) where two directions, a and b, have a finite resultant vorticity while the third c direction does not. Congruently, the a and b directions have a positive reorientational entropy, while a negative entropy is found in the c direction.

What happens at lower temperatures, i.e., for $T < T_3$, is still under study. For example, while we expect the system to naturally proceed towards an isotropic lattice through what should be a rhombohedral phase, an unexpected structural change occurs at $T \simeq 125$ K [19], a rearrangement that is also detected in dielectric spectroscopy data [see Figs. 3(b) and 3(c)].

Since $KTa_{0.64}Nb_{0.36}O_3$ (KTN) is a variant of other solid solution potassium-based perovskites that are relaxors, our study sheds light on the role played by topological defects in determining complexity-driven phenomena and nonergodicity. In the language of relaxor physics, the average ordered high T perovskite structure can host a population of uncorrelated polar nanoregions (PNR) [31]. Upon cooling, different PNRs start to interact persistently with each other and, below the Curie temperature, they can produce self-organized macroscopic polarization domains. The 3D vortex pattern is then that PNR structure that screens volume and surface charge and minimizes stress, while different vortices can self-organize into the SC that eventually occupies the whole bulk volume. It is this mesoscale structure of polarization domains that ultimately lowers the average lattice symmetry at the atomic scale, producing an anisotropic chiral stress field that induces the detectable orthorhombic distortion deep in the tetragonal phase, a remarkably strong microscopic-macroscopic correlation that binds x-ray data to dielectric spectroscopy data.

Summary. Temperature resolved x-ray diffraction experiments in KTN signal a violation of the conventional perovskite sequence of lattice symmetries on cooling below the Curie temperature. The observed sequence indicates that the symmetry of the average atomic structure can increase on cooling and the cell structure can manifest negative-to-zero thermal volume expansion. Dielectric measurements, calorimetry, optical diffraction, and second-harmonic generation experiments suggest that the anomaly is associated to a coherent lattice distortion driven by strain relaxation to a ferroelectric supercrystal, a 3D superlattice of interwoven polarization vortices.

[1] Z. B. Guo, Y. W. Du, J. S. Zhu, H. Huang, W. P. Ding, and D. Feng, Large Magnetic Entropy Change in Perovskite-Type Manganese Oxides, Phys. Rev. Lett. **78**, 1142 (1997).

[2] B. G. Kim, S. M. Cho, T. Y. Kim, and H. M. Jang, Giant Dielectric Permittivity Observed in Pb-Based Perovskite Ferroelectrics, Phys. Rev. Lett. **86**, 3404 (2001).

[3] J. Wu, J. W. Lynn, C. J. Glinka, J. Burley, H. Zheng, J. F. Mitchell, and C. Leighton, Intergranular Giant Magnetoresistance in a Spontaneously Phase Separated Perovskite Oxide, Phys. Rev. Lett. **94**, 037201 (2005).

[4] R. Mahjoub, S. P. Alpay, and V. Nagarajan, Theory of Giant Electromechanical Response from Ferroelectric Bilayers with Polydomain Structures due to Interlayer and Interdomain Coupling, Phys. Rev. Lett. **105**, 197601 (2010).

[5] C. W. Hicks, D. O. Brodsky, E. A. Yelland, A. S. Gibbs, J. A. N. Bruin, M. E. Barber, S. D. Edkins, K. Nishimura, S. Yonezawa, Y. Maeno, and A. P. Mackenzie, Strong increase of T_c of Sr_2RuO_4 under both tensile and compressive strain, Science **344**, 283 (2014).

[6] W. S. Yang, B.-W. Park, H. Jung, N. J. Jeon, Y. C. Kim, D. U. Lee, S. S. Shin, J. Seo, E. K. Kim, J. H. Noh, and S. I. Seok, Iodide management in formamidinium-lead-halide-based perovskite layers for efficient solar cells, Science **356**, 1376 (2017).

[7] S. Liu, and R. E. Cohen, Origin of Negative Longitudinal Piezoelectric Effect, Phys. Rev. Lett. **119**, 207601 (2017).

[8] F. Di Mei, L. Falsi, M. Flammini, D. Pierangeli, P. Di Porto, A. J. Agranat, and E. DelRe, Giant broadband refraction in the visible in a ferroelectric perovskite, Nat. Photon. **12**, 734 (2018).

[9] H. Ma, C. Li, Y. W. Ma, H. Wang, Z. W. Rouse, Z. L. Zhang, C. Slebodnick, A. Alatas, S. P. Baker, J. J. Urban, and Z. T. Tian, Supercompliant and Soft $(CH_3NH_3)_3Bi_2I_9$ Crystal with Ultralow Thermal Conductivity, Phys. Rev. Lett. **123**, 155901 (2019).

[10] P. Torres, J. Iniguez, and R. Rurali, Giant Electrophononic Response in $PbTiO_3$ by Strain Engineering, Phys. Rev. Lett. **123**, 185901 (2019).

[11] L. Falsi, L. Tartara, F. Di Mei, M. Flammini, J. Parravicini, D. Pierangeli, G. B. Parravicini, F. Xin, P. DiPorto, A. J. Agranat, and E. DelRe, Constraint-free wavelength conversion supported by giant optical refraction in a 3D perovskite supercrystal, Commun. Mater. **1**, 76 (2020).

[12] H. Cui, R. Hensleigh, D. Yao, D. Maurya, P. Kumar, M. G. Kang, S. Priya, and X. (R.) Zheng, Three-dimensional printing of piezoelectric materials with designed anisotropy and directional response, Nat. Mater. **18**, 234 (2019).

[13] C. Zhu, X. Niu, Y. Fu, N. Li, C. Hu, Y. Chen, X. He, G. Na, P. Liu, H. Zai, Y. Ge, Y. Lu, X. Ke, Y. Bai, S. Yang, P. Chen, Y. Li, M. Sui, L. Zhang, H. Zhou, and Q. Chen, Strain engineering in perovskite solar cells and its impacts on carrier dynamics, Nat. Commun. **10**, 815 (2019).

[14] L. Martiradonna, Riddles in perovskite research, Nat. Mater. **17**, 377 (2018).

[15] D. Pierangeli, M. Ferraro, F. Di Mei, G. Di Domenico, C. E. M. de Oliveira, A. J. Agranat, and E. DelRe, Supercrystals in composite ferroelectrics, Nat. Commun. **7**, 10674 (2016).

[16] M. Ferraro, D. Pierangeli, M. Flammini, G. Di Domenico, L. Falsi, F. Di Mei,, A. J. Agranat, and E. DelRe, Observation of polarization-maintaining light propagation in depoled compositionally disordered ferroelectrics, Opt. Lett. **42**, 3856 (2017).

[17] X. Zhang, Q. X. Yang, H. L. Liu, X. P. Wang, S. He, X. J. Li, and P. F. Wu, Switching effects of spontaneously formed superlattices in relaxor ferroelectrics, Opt. Mat. Express **9**, 4081 (2019).

[18] F. Jona and G. Shirane, *Ferroelectric Crystals* (Dover publishing, New York, 1993).

[19] See Supplemental Material at http://link.aps.org/supplemental/10.1103/PhysRevB.102.214110, Fig. S2 for further experimental data, "Single-crystal x-ray diffraction" section for a full discussion of technical details and procedures employed in selecting the samples and obtaining accurate lattice parameters, "Directional dielectric spectroscopy" section, for a detailed description about anisotropicity in dielectric response, Figs. S2–S7 for further experimental data about orientation of lattice parameters, Table S-III for further experimental data about lattice parameters, "Vorticity in SCs" and "Vortex strain" sections for a detailed description about the 3D SC strain and vorticity, "Trend of Cell Parameters" section for a detailed description about the evolution of cell parameters, "Second-Harmonic-Generation" section for a detailed description about second-harmonic-generation process in this kind of crystal, "Fröhlich Entropy" section, for a detailed description about order-disorder features by dielectric measurements, and Figs. S4–S6 for further experimental data on structural changes.

[20] R. Destro, R. Ruffo, P. Roversi, R. Soave, L. Loconte, and L. Lo Presti, Anharmonic motions versus dynamic disorder at the Mg ion from the charge densities in pyrope $(Mg_3Al_2Si_3O_{12})$ crystals at 30 K: six of one, half a dozen of the other, Acta Crystallogr. Sect. B **73**, 722 (2017).

[21] R. Destro, E. Sartirana, L. Loconte, R. Soave, P. Colombo, C. Destro, L. Lo Presti, Competing $C = O \cdots C - O$, $C - H \cdots O$, $Cl \cdots O$, and $Cl \cdots Cl$ interactions governing the structural phase transition of 2, 6-dichloro-p-benzoquinone at $T_c = 122.6$ K, Crystal Growth and Design **13**, 4571 (2013).

[22] R. Destro, E. Ortoleva, R. Soave, L. Loconte, and L. Lo Presti, Detection and kinetics of the single-crystal to single-crystal complete transformation of a thiiranium ion into thietanium ion, PCCP **11**, 7181 (2009).

[23] L. Lo Presti, M. Allieta, M. Scavini, P. Ghigna, L. Loconte, V. Scagnoli, and M. Brunelli, Crystal structure and structural phase transitions in the $GdBaCo_2O_{5.0}$ cobaltite, Phys. Rev. B **84**, 104107 (2011).

[24] SMART and SAINT-Plus. Bruker AXS Inc., Madison, Wisconsin (2012).

[25] L. Lo Presti, D. Invernizzi, R. Soave, and R. Destro, Looking for structural phase transitions in the colossal magnetoresistive thiospinel $FeCr_2S_4$ by a multi-temperature single-crystal X-ray diffraction study, Chem. Phys. Lett. **416**, 28 (2005).

[26] X. Wang, J. Wang, Y. Yu, H. Zhang, and R. I. Boughton, Growth of cubic $KTa_{1-x}Nb_xO_3$ crystal by Czochralski method, J. Cryst. Growth **293**, 398 (2006).

[27] B. Zalar, A. Lebar, J. Seliger, R. Blinc, V. Laguta, and M. Itoh, NMR study of disorder in $BaTiO_3$ and $SrTiO_3$, Phys. Rev. B **71**, 064107 (2005).

[28] B. Zalar, V. V. Laguta, and R. Blinc, NMR Evidence for the Coexistence of Order-Disorder and Displacive Components in Barium Titanate, Phys. Rev. Lett. **90**, 037601 (2003).

[29] A. Agranat, R. Hofmeister, and A. Yariv, Characterization of a new photorefractive material: $K_{1-y}L_yT_{1-x}N_x$, Opt. Lett. **17**, 713 (1992).

[30] J. Toulouse, The three characteristic temperatures of relaxor dynamics and their meaning, Ferroelectrics **369**, 203 (2008).

[31] A. Bokov, Recent progress in relaxor ferroelectrics with perovskite structure, J. Mater. Sci. **41**, 31 (2006).

[32] A. W. Hewat, Cubic-tetragonal-orthorhombic-rhombohedral ferroelectric transitions in perovskite potassium niobate: neutron powder profile refinement of the structures, J. Phys. C: Solid State Phys. **6**, 2559 (1973).

[33] X. R. Huang, S. S. Jiang, A. Y. Xu, J. Y. Wang, Q. C. Guan, J. H. Jiang, and D. Feng, Ferroelectric domain structures and phase transitions in $KTa_{1-x}Nb_xO_3$ crystals, Phys. Status Solidi A **148**, 611 (1995).

[34] E. Bouziane, M. Fontana, and W. Kleeman, A study of the successive phase transitions in $KTa_{0.93}Nb_{0.07}O_3$ by light scattering, dielectric permittivity and light diffraction measurement, J. Phys.: Condens. Matter **6**, 1965 (1994).

[35] G. Shirane, and A. Takeda, Transition energy and volume change at three transitions in barium titanate, J. Phys. Soc. Jpn. **7**, 1 (1952).

[36] D. Rytz, and H. J. Scheel, Crystal growth of $KTa_{1-x}Nb_xO_3$ ($0 < x \leqslant 0.04$) solid solutions by a slow-cooling method, J. Cryst. Growth **59**, 468 (1982).

[37] E. D. Politova, E. A. Fortalnova, G. M. Kaleva, A. V. Mosunov, M. G. Safronenko, N. U. Venskovskii, V. V. Shvartsman, and W. Kleemann, Ferroelectric phase transitions and electroconducting properties of ceramic BIMEVOX solid solutions (Me=La, Zr), Ferroelectrics **391**, 3 (2009).

[38] V. V. Shvartsman and D. C. Lupascu, Lead-free relaxor ferroelectrics, J. Am. Ceram. Soc. **95**, 1 (2012).

[39] J. Parravicini, E. DelRe, A. J. Agranat, and G. B. Parravicini, Liquid-solid directional composites and anisotropic dipolar phases of polar nanoregions in disordered perovskite, Nanoscale **9**, 9572 (2017).

[40] J.-C. Tolédano, J.-C., V. Janovec, V. Kopský, J. F. Scott, P. Boček, Structural phase transitions, Vol. D, Chap. 3.1, pages 338–376 of *International Table for Crystallography* (Springer, Dordrecht, Netherlands, 2006).

[41] K. Aizu, Possible species of ferromagnetic, and ferroelectric, and ferroelastic crystals, Phys. Rev. B **2**, 754 (1970).

[42] A. Bokov and Z. Ye, Reentrant phenomena in relaxors, *Nanoscale ferroelectrics and multiferroics: Key Processing and Characterization Issues, and Nanoscale Effects, Volumes I and II* (Wiley, New York, 2016), Chap. 23.

[43] R. Comès, M. Lambert, and A. Guinier, Désordre linéaire dans las cristaux (cas du Silicium, du Quartz, et des Pérovskites Ferroélectriques), Acta Crystallogr. Sect. A **26**, 244 (1970).

[44] J. Parravicini, E. DelRe, A. J. Agranat, and G. B. Parravicini, Macroscopic response and directional disorder dynamics in chemically substituted ferroelectrics, Phys. Rev. B **93**, 094203 (2016).

[45] A. L. Roytburd, J. Ouyang, and A. Artemev, Polydomain structures in ferroelectric and ferroelastic epitaxial films, J. Phys.: Condens. Matter **29**, 163001 (2017).

[46] P. W. Forsbergh, Domain Structures and Phase Transitions in Barium Titanate, Phys. Rev. **76**, 1187 (1949).

[47] J. Sapriel, Domain-wall orientation in ferroelastics, Phys. Rev. B **12**, 5128 (1975).

[48] M. Alguero, J. M. Gregg, and L. Mitoseriu (Eds.) *Nanoscale Ferroelectrics and Multiferroics* (Wiley, Hoboken, USA, 2016), Chap. 22.

[49] V. A. Stoica, N. Laanait, C. Dai, Z. Hong, Y. Yuan, Z. Zhang, S. Lei, M. R. McCarter, A. Yadav, A. R. Damodaran, S. Das, G. A. Stone, J. Karapetrova, D. A. Walko, X. Zhang, L. W. Martin, R. Ramesh, L.-Q. Chen, H. Wen, V. Gopalan, and J. W. Freeland, Optical creation of a supercrystal with three-dimensional nanoscale periodicity, Nat. Mater. **18**, 377 (2019).

[50] S. Das, Y. L. Tang, Z. Hong, M. A. P. Gonçalves, M. R. McCarter, C. Klewe, K. X. Nguyen, F. Gómez-Ortiz, P. Shafer, E. Arenholz, V. A. Stoica, S.-L. Hsu, B. Wang, C. Ophus, J. F. Liu, C. T. Nelson, S. Saremi, B. Prasad, A. B. Mei, D. G. Schlom, J. Íñiguez, P. García-Fernández, D. A. Muller, L. Q. Chen, J. Junquera, L. W. Martin, and R. Ramesh, Observation of room-temperature polar skyrmions, Nature (London) **568**, 368 (2019).

[51] J. Wang, K. Nagano, T. Shimada, and T. Kitamura, Strain-mediated multilevel ferroelectric random access memory operating through a magnetic field, RSC Adv. **4**, 45382 (2014).

[52] I. Muench, A. Renuka Balakrishna, J. E. Huber, Periodic boundary conditions for the simulation of 3D domain patterns in tetragonal ferroelectric material, Arch. Appl. Mech. **89**, 955 (2019).

[53] K. Wang, and J.-F. Li, Analysis of crystallographic evolution in $(Na, K)NbO_3$-based lead-free piezoceramics by x-ray diffraction, Appl. Phys. Lett. **91**, 262902 (2007).

[54] S. A. Borisov, S. B. Vakhrushev, E. Y. Koroleva, A. A. Naberezhnov, P. P. Syrnikov, V. G. Simkin, Z. Kutnjak, V. Egami, W. Dmowski, and P. Piekarz, Investigation into the evolution of the structure of $K_{1-x}Li_xTa_{1-y}Nb_yO_3$ single crystals under variations in temperature, Crystallogr. Rep. **52**, 440 (2007).

[55] H. Abe, K. Harada, R. J. Matsuo, H. Uwe, and K. Ohshima, X-ray diffuse scattering associated with ferroelectric microregions in $KTa_{1-x}Nb_xO_3$, J. Phys.: Condens. Matter **13**, 3257 (2001).

[56] P. M. Gehring, H. Chou, S. M. Shapiro, J. A. Hriljac, D. H. Chen, J. Toulouse, D. Rytz, and L. A. Boatner, Dipole-glass behavior of lightly doped $KTa_{1-x}Nb_xO_3$, Phys. Rev. B **46**, 5116 (1992).

[57] A. K. Yadav, K. X. Nguyen, Z. Hong, P. García-Fernández, P. Aguado-Puente, C. T. Nelson, S. Das, B. Prasad, D. Kwon, S. Cheema, A. I. Khan, C. Hu, J. Íñiguez, J. Junquera, L.-Q. Chen, D. A. Muller, R. Ramesh, and S. Salahuddin, Spatially resolved steady-state negative capacitance, Nature (London) **565**, 468 (2019).

[58] M. Hoffmann, F. P. G. Fengler, M. Herzig, T. Mittmann, B. Max, U. Schroeder, R. Negrea, P. Lucian, S. Slesazeck, and T. Mikolajick, Unveiling the double-well energy landscape in a ferroelectric layer, Nature (London) **565**, 464 (2019).

[59] P. K. Tien, R. Ulrich, and R. J. Martin, Optical second harmonic generation in form of coherent Cerenkov radiation from a thin-film waveguide, Appl. Phys. Lett. **17**, 447 (1970).

[60] Y. Sheng, A. Best, H.-J. Butt, W. Krolikowski, A. Arie, and K. Koynov, Three-dimensional ferroelectric domain visualization by Cerenkov-type second harmonic generation, Opt. Exp. **18**, 16539 (2010).

[61] M. Azuma, W. Chen, H. Seki, M. Czapski, S. Olga, K. Oka, M. Mizumaki, T. Watanuki, N. Ishimatsu, N. Kawamura, S. Ishiwata, M. G. Tucker, Y. Shimakawa, and J. P. Attfeld, Colossal negative thermal expansion in $BiNiO_3$ induced by intermetallic charge transfer, Nat. Commun. **2**, 347 (2011).

[62] J. D. Dunitz, Phase transitions in molecular crystals: looking backwards, glancing sideways, Phys. Scr. **91**, 112501 (2016).

[63] Y. V. Mnyukh, Molecular mechanism of polymorphic transitions, Mol. Cryst. Liq. Cryst. **52**, 163 (1979).

[64] S. Triebwasser, Study of ferroelectric transitions of solid-solution single crystals of $KNbO_3$-$KTaO_3$, Phys. Rev. **114**, 63 (1959).

[65] A. A. Bokov, and Z.-G. Ye, Dielectric relaxation in relaxor ferroelectrics, J. Adv. Dielect. **2**, 1241010 (2012).

[66] P. Tan, H. Tian, F. Huang, X. Meng, Y. Wang, C. Hu, X. Cao, L. Li, and Z. Zhou, Strain-Gradient-Controlled Disorder Dynamics in Chemically Substituted Ferroelectrics, Phys. Rev. Appl. **11**, 024037 (2019).

[67] J. Parravicini, P. Minzioni, V. Degiorgio, E. DelRe, Observation of nonlinear Airy-like beam evolution in lithium niobate, Opt. Lett. **34**, 3908 (2009).

[68] J. Parravicini, F. Di Mei, C. Conti, A. J. Agranat, E. DelRe, Diffraction cancellation over multiple wavelengths in photorefractive dipolar glasses, Opt. Express **19**, 24109 (2011).

[69] J. Parravicini, C. Conti, A. J. Agranat, E. DelRe, Rejuvenation in scale-free optics and enhanced diffraction cancellation lifetime, Opt. Express **20**, 27382 (2012).

[70] G. P. Johari, Effects of electric field on the entropy, viscosity, relaxation time, and glass-formation, J. Chem. Phys. **138**, 154503 (2013).

[71] L. Landau and E. Lifshitz, *Electrodynamics of Continuous Media* (Pergamon Press, Oxford, UK, 1960).

[72] J. Nye, *Physical Properties of Crystals - Their Representation by Tensors and Matrices* (Clarendon Press, Oxford, UK, 1985).

[73] A. F. Devonshire, Theory of ferroelectrics, Adv. Phys. **3**, 85 (1954).

[74] H. Fröhlich, *Theory of Dielectrics*, 2nd ed. (Clarendon Press, Oxford, 1958).

[75] A. Sassella, D. Braga, M. Campione, T. Ciabattoni, M. Moret, J. Parravicini, and G. B. Parravicini, Probing phase transitions and stability of organic semiconductor single crystals by dielectric investigation, J. Appl. Phys. **109**, 013529 (2011).

[76] J. Parravicini, Thermodynamic potentials in anisotropic and nonlinear dielectrics, Physica B **541**, 54 (2018).